



Multiple infrared bands absorber based on multilayer gratings

Xiaoyi Liu ^{a,b}, Jinsong Gao ^{a,b}, Haigui Yang ^{a,*}, Xiaoyi Wang ^a, Chengli Guo ^{a,b}

^a Key Laboratory of Optical System Advanced Manufacturing Technology, Changchun Institute of Optics, Fine Mechanics and Physics, Chinese Academy of Sciences, Changchun 130033, China

^b University of the Chinese Academy of Sciences, Beijing 100039, China



ARTICLE INFO

Keywords:

Multilayer gratings
Infrared atmospheric windows
Fabry–Perot resonance
Surface plasmon polaritons

ABSTRACT

The present study offers an Ag/Si multilayer-grating microstructure based on an Si substrate. The microstructure exhibits designable narrowband absorption in multiple infrared wavebands, especially in mid- and long-wave infrared atmospheric windows. We investigate its resonance mode mechanism, and calculate the resonance wavelengths by the Fabry–Perot and metal–insulator–metal theories for comparison with the simulation results. Furthermore, we summarize the controlling rules of the absorption peak wavelength of the microstructure to provide a new method for generating a Si-based device with multiple working bands in infrared.

© 2017 Elsevier B.V. All rights reserved.

1. Introduction

At present, mid- and long-wave infrared spectral ranges have become the major working bands of various advanced technologies: with the utilization of the widely infrared spectrum, solar cells based on thermal energy conversion can offer higher energy conversion efficiency as compared to traditional photovoltaics [1]; and obtaining an object's infrared emission at multiple wavelengths can be used to filter background noise, thereby allowing reconstruction of the object's absolute temperature [2]. The 3–5 μm and 8–14 μm wavebands respectively represent the mid- and long-wave infrared (MWIR and LWIR, respectively) atmospheric windows, which provide working bands for detectors without interferences from dust, water vapor, or other atmospheric influences [3]. As a result, the functions of optical imaging devices or detectors are sufficiently exerted in atmospheric windows and produce a variety of astronomical, thermographic, surveillance, and automotive safety applications [3].

However, the detection of multiple wavebands generally requires a series of detectors and a correspondingly complicated electronic and optical system, thereby resulting in a high cost and high technological level requirements [2]. The exploration of a single detector with multiple response bands is a feasible approach to avoid the above issue given that the brunt of the vision is limited to the selection of an appropriate material for the preparation of imaging devices or detectors. Semiconductor Si can be considered as a candidate due to its outstanding advantages such as its low price, high performance, and mature technology [4–7]. However, the response range of Si-based

optoelectronic devices mainly focuses on the visible spectrum due to its wide intrinsic band gap (1.12 eV) [8,9]. Therefore, it is necessary to extend its response range into the infrared region, especially with MWIR and LWIR atmospheric windows.

Plasmonics induced by metal microstructures that are covered on or embedded in semiconductors have been widely investigated to extend the response range of Si-based optoelectronic devices [10–15]. With the aid of the plasmonic effect, the potential barrier height at the metal/semiconductor interface becomes the limiting factor of the response region rather than the bandgap of the semiconductor substrate [16–20], thereby offering a possibility of extending the working band of the Si-based device. Accordingly, the present study offers a multilayer-grating microstructure alternately consisting of Ag and Si layers, which not only produces a grating-excited plasmonic effect but also permits a linear designable responsivity peak within a broad waveband. As compared to traditional grating-shaped microstructures, we used alternating Ag–Si layers to replace single-material gratings, and realized the multiple infrared band response through the laminated structure-induced Fabry–Perot (F–P) cavity. The detailed results and investigations are presented below.

2. Simulation modeling

The structure of the multilayer grating was composed of five alternating layers that covered the Si substrate, including two 100-nm-thick Si layers and three 50-nm-thick Ag layers, with a grating constant of

* Corresponding author.

E-mail addresses: gaojs@ciomp.ac.cn (J. Gao), yanghg@ciomp.ac.cn (H. Yang).

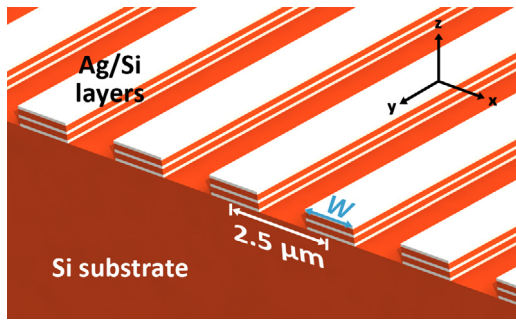


Fig. 1. Diagram of the designed multilayer-grating microstructure.

2.5 μm (Fig. 1). The present study employed the finite-difference-time-domain (FDTD) method to analyze the designed multilayer grating, and the optimization process of each layer's number and thickness will be discussed in the corresponding section of Fig. 3. All parameters mentioned above were optimized except for the width of each stripe (W), which can observably influence its peak wavelength position in the absorption spectrum. Our simulations adopted an x -polarized plane wave as the incidence source. In the case of normal incidence, the periodic condition was set as the boundary condition of both the x - and y -directions, whereas the Bloch condition was adopted under oblique incidence. In the z -direction, the perfectly matched layer (PML) condition was adopted to measure the transmittance (T) and reflectance (R), such that the extracting absorptance (A) is defined as $A = 1 - T - R$. Meanwhile, a high mesh accuracy of 2 nm was also adopted to guarantee the convergence of the simulations, and a series of repeated simulations were calculated to verify its stability. All the above aspects were considered in the modeling to ensure the reliability of the following calculations.

3. Results and discussion

Fig. 2(a) presents the dependence of the simulated absorption curves on variable W of the multilayer-grating microstructures under a normal incidence source, wherein the absorption spectrum is comprised of two ranges. An increasing in W from 1.1 μm to 1.6 μm tuned the absorption peak wavelength from 3.2 μm to 4.6 μm in the MWIR band, and from 9.5 μm to 13.8 μm in the LWIR band, which correspond to the two infrared atmospheric windows. This calculation suggests that two narrowband absorption peaks of the designed multilayer grating can be controlled simultaneously by shifting the stripe's width W into two focused infrared working bands, thereby generating an Si-based dual infrared response band device. The redshift phenomenon corresponds with the general law

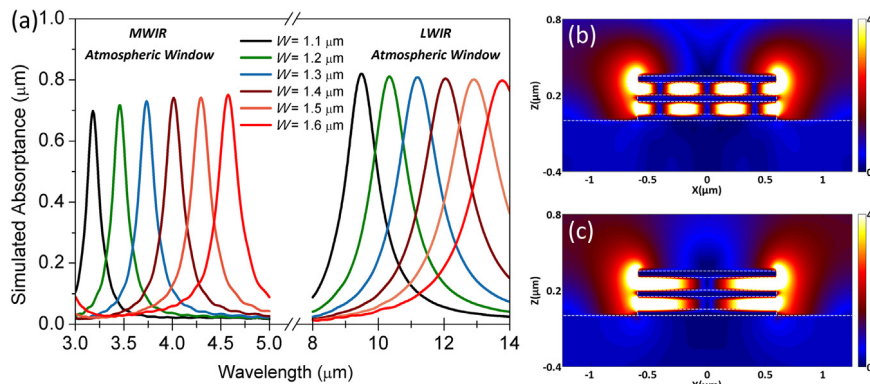


Fig. 2. (a) Dependence of the simulated absorptance on the W of the multilayer gratings. (b) and (c) Longitudinal (xz -plane) electric-field intensity distributions of the microstructures with $W = 1.2 \mu\text{m}$ at an incident wavelength of 3.45 μm and 10.33 μm, respectively. The color bars represent the relative electric field intensity (E/E_0).

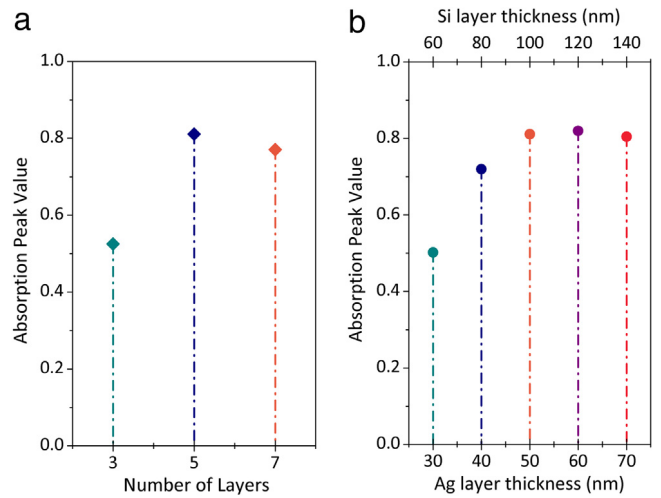


Fig. 3. (a) and (b) Dependence of the simulated absorption peak value of the mode in the LWIR band on the layer number and layer thickness of the multilayer-grating microstructure.

of grating-shaped microstructure [11,12,18]. However, its mechanism requires further investigation and discussion.

Fig. 2(b) and (c) present the longitudinal electric-field intensity distributions of the microstructure with $W = 1.2 \mu\text{m}$ when the incident light wavelengths were at 3.45 μm and 10.33 μm, respectively, which precisely corresponds to the two peak wavelengths of the absorption curves in Fig. 2(a). The color bars represent the relative electric field intensity, which is standardized by the incident electric field intensity (E/E_0). Based on a comparison of the two pictures, the energies converged in the Si layers both exhibited a nodal distribution mode that was composed of alternating bright and dark regions. However, manifest distinctions were observed between these regions due to the formation of Si layer-induced transverse F-P cavities, which induced diverse energy distribution modes at different but suitable incident wavelengths. The surface plasmon polaritons (SPPs) by the grating-shaped structure were first excited at the Ag-Si interfaces, wherein the penetration depths on the metal side were much smaller than the depths on the Si side, thereby resulting in confining energies within the Si layers [21]. Meanwhile, the SPPs propagating along the interfaces formed standing waves between two Si-vacuum interfaces. As a result, the energies exhibited transverse nodal arrangement modes within the interfaces. It is a typical F-P cavity system with a frequency-sensitive characteristic that only the frequency-matched SPPs are able to produce standing waves by coherent superposition [22–24], which explains the difference in the distribution modes of the electric-field intensity and the corresponding dual narrowband absorption peaks.

The present study further investigated the dependence of the simulated absorption peak value of the strongest mode in the LWIR band on the layer number and layer thickness of the multilayer-grating microstructure with a width of $W = 1.2 \mu\text{m}$, as presented in Fig. 3(a) and (b), respectively. An increase in the layer number or thickness tended to exhibit a saturated absorptance, and even has a slight decrease. Therefore, five layers containing three 50-nm-thick Ag layers and two 100-nm-thick Si layers were determined to be the best formation for the simulations. As for the grating constant, the simulation results indicated that as the period length shifts within a specific range, the absorptance remained virtually unchanged.

Owing to the regularity of designed Ag–Si laminated structure, we can describe it mathematically by metal–insulator–metal (MIM) and F–P cavity theories. A general resonance condition for this waveguide was first defined as follows [25,26]:

$$2W\beta + \varphi_r = 2m\pi \quad (1)$$

where β is the complex propagation constant, m is the resonance order, φ_r is the phase shift of the propagating waves at the two facets of the waveguide, and W is the width of the grating stripe, which represents the length of the F–P cavity. The resonance order m can be calculated using Eq. (1) and the value of β . Fortunately, the complex propagation constant β can be obtained from the following dispersion equations, which are based on the waveguide theory [25,27]:

$$\begin{aligned} \varepsilon_d k_m + \varepsilon_m k_d \tanh\left(\frac{k_d h}{2}\right) &= 0 \\ \beta^2 - \varepsilon_d k_0^2 &= k_d^2 \\ \beta^2 - \varepsilon_m k_0^2 &= k_m^2 \end{aligned} \quad (2)$$

where ε_d and ε_m are the dielectric constants of Si and Ag, respectively, h is the thickness of the Si layers (100 nm), and $k_0 = 2\pi/\lambda$ is the free space wave vector. The values of β were calculated according to the preceding steps to obtain the resonance order m . A microstructure with a width of $W = 1.2 \mu\text{m}$ has a resonance order of 3 or 1 when the incident light wavelengths are at 3.45 μm and 10.33 μm , respectively. Therefore, the energy distribution in Fig. 2(b) was defined as mode 3 and the distribution in Fig. 2(c) was defined as mode1.

Based on the presented concept of modes, the multilayer grating was assumed to exhibit higher order energy distribution modes. To validate this assumption, we subsequently calculated the absorptance of the designed structure with $W = 1.2 \mu\text{m}$ in a relatively large wavelength range (Fig. 4). The broadband absorption curve in Fig. 4 validated the presence of higher order modes and several absorption peaks in primarily atmospheric windows that contained near infrared (NIR), MWIR, and LWIR ranges, thereby allowing the designed microstructure to simultaneously fulfill and regulate a multiband response. The latter two windows were still characterized as major operation bands for the presented structure given their higher absorption peaks. Furthermore, these peak wavelengths can be quantitatively derived. The effective refractive index n_e of the MIM waveguide was introduced as $n_e = \beta/k_0$ to derive the resonance wavelength λ_r according to the above mathematical model, wherein the resonance wavelength λ_r can be expressed as follows [25,28]:

$$\lambda_r = 2n_e W / (m - \varphi_r / 2\pi) \quad (3)$$

where λ_r can be easily calculated following the substitution of n_e and m into the above equation. According to Eq. (3), the peak wavelengths are proportional to W , which clarifies the aforementioned redshift phenomenon. In addition, Eq. (3) can be used to quantitatively compare and verify the results of the FDTD simulations. It is important to note that the phase shift term $\varphi_r / 2\pi$ remains in the denominator of Eq. (3) and greatly influences the λ_r term such that it cannot be regarded as a constant for different wavelengths [28]. In the concrete calculations, the values of φ_r were first calculated for $m = 1$ (1.176) and $m = 3$ (3.474) based on the above equations. The phase shift values of mode 5 (5.772)

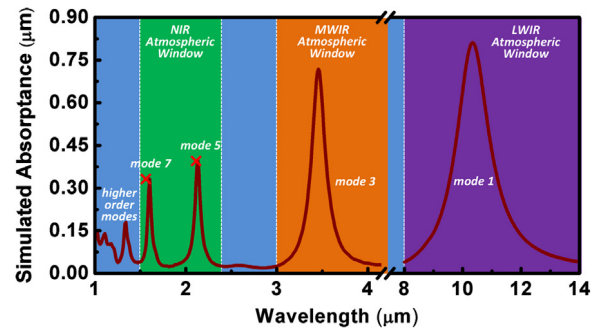


Fig. 4. Broadband-simulated absorptance of the multilayer-grating microstructure with $W = 1.2 \mu\text{m}$. The red symbol “x” represents the resonance wavelength calculated by Eq. (3).

and mode 7 (8.070) were then respectively obtained based on these two values and by a linear fitting (LF) method, of which their resonance wavelengths λ_r were subsequently derived to compare with the FDTD simulations. The calculation results are marked in Fig. 4 by the red symbol “x”. The results derived by Eq. (3) were well in agreement with those by the FDTD simulations, and any small deviations may be a result of the inappropriate fitting method employed for the phase shift.

Additionally, Fig. 5 exhibits the presence of odd modes and the corresponding absence of even modes in the absorption curve. This phenomenon may be related to symmetry constraints: in the case of oblique incidence, in addition to the odd modes, the missing even modes which are not excitable before can be observed [27]. Fig. 5(a) presents a comparison of the absorptance between normal and oblique (45°) incident sources, wherein two new absorption peaks, or resonance modes, were observed under the oblique source. Fig. 5(b) and (c) present the longitudinal electric-field intensity distributions for oblique incident light wavelengths of 2.62 μm and 5.18 μm , which precisely correspond to the two new resonance wavelengths. The color bars represent the relative electric field intensity (E/E_0). The new modes can also be quantitatively investigated by the above equations, specifically by successively deriving β , m , φ_r , and λ_r . We also adopted a quadratic curve fitting (QCF) method to fit the phase shift φ_r , which requires other three phase shift values, for comparison with the LF method. The present study first confirmed the resonance order m of the new mode ($m = 2$) between modes 1 and 3, and fit its phase shift according to other two values of φ_r ($m = 1$, and 3; LF method) and other three values of φ_r ($m = 1, 3$, and 5; QCF method), respectively. Different resonance wavelengths were then derived through Eq. (3), of which the calculation results are marked in Fig. 5 by a red symbol “x” (calculated by the LF method) and a blue symbol “x” (calculated by the QCF method). According to the inset, the LF method-calculated results were closer to the FDTD results than those by the QCF method-calculated results, thereby indicating that a higher fitting order does not correlate to better results. Unlike mode 2, we were unable to follow these steps to quantitatively describe mode 4 due to the presence of a “jump area” in the vicinity of the 2.5 μm waveband, because the complex propagation constant β exhibited a leaping change in this waveband. Therefore, it is difficult to obtain a stable numerical solution for mode 4 by solving the dispersion equations as it results in an inaccessible resonance wavelength.

Moreover, defining “ λ_{spp} ” as the plasmon wavelength, which is determined by the cavity length divided by the mode order [27], presents a correlation between the plasmon wavelength and the wavelength of the absorption peak, or the resonance wavelength. According to Fig. 6, an approximately linear dependency belonging to different modes was observed between the peak wavelengths and λ_{spp} . In other words, the peak positions are largely dependent upon the concept of the plasmon wavelength. This interesting conclusion provides another reasonable and intuitive explanation for the redshift phenomenon in Fig. 2(a): for a given mode, the plasmon wavelength λ_{spp} increased following

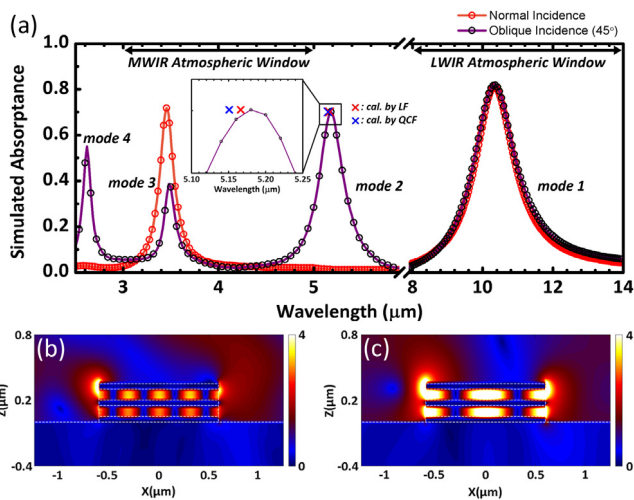


Fig. 5. (a) Comparison of the simulated absorbance between the normal and oblique (45°) incident sources. The red and blue “x” symbols represent the resonance wavelengths calculated by Eq. (3) within the different phase shift fitting methods for a stripe width (W) of 1.2 μm . (b) and (c) Longitudinal (xz -plane) electric-field intensity distributions of the microstructures with $W = 1.2 \mu\text{m}$ at an oblique incident wavelength of 2.62 μm and 5.18 μm , respectively. The color bars represent the relative electric field intensity (E/E_0).

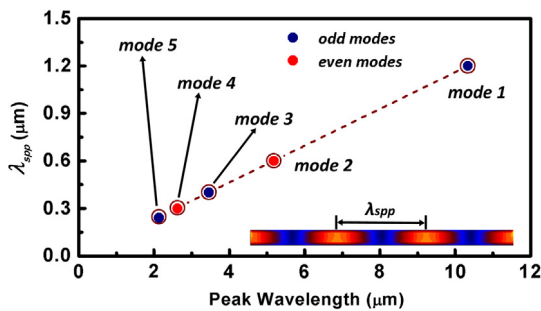


Fig. 6. Dependence of the plasmon wavelength λ_{spp} on absorption peak wavelength.

an increase in W , and the absorption peak wavelength exhibited a consequential linear red shift. The plasmon wavelength also presented another characteristic; specifically, it equaled the distance of two neighboring antinodes in electric-field intensity figures. Both odd and even modes were consistent with this rule, thereby allowing rapid judgments on its resonance mode only by the electric-field intensity distribution, and thus avoiding complicated calculations.

Finally, Fig. 7 summarizes the absorbance of our microstructures under normal incidence with various W values in several major atmospheric windows. A change in the stripe width W generated high average absorbances (around 70%–80%) in mode 1 and mode 3 that covered the entirety of the LWIR (8–14 μm) and MWIR (3–5 μm) atmospheric windows, respectively, thereby allowing simultaneous shifts in the multilayer grating’s response peaks in both the LWIR and MWIR bands. Certain higher order modes appeared without particularly prominent absorption in the NIR spectrum (1.5–2.4 μm). Therefore, the designed multilayer grating formulated a function for the multiple infrared bands response. In addition, we could simultaneously shift its response bands to our interested ranges by changing the grating width W , which offers a new perspective for controlling and regulating the device’s working bands in the infrared atmospheric windows. Furthermore, it is remarkable that the jump area also appeared in the vicinity of 2.5 μm waveband, thereby resulting in the break of mode 5.

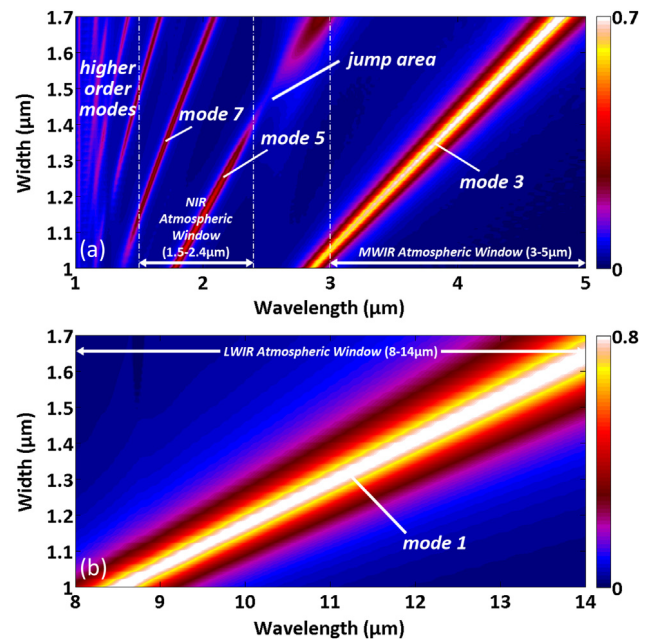


Fig. 7. (a) and (b) Summary of the absorption spectrum of the multilayer-grating microstructures with various stripe widths (W). The color bar represents the relative absorbance.

4. Conclusion

In summary, the present study offered an Ag/Si multilayer-grating microstructure that covered a Si substrate, of which its parameters were optimized to enhance its absorption. In MWIR and LWIR atmospheric windows (3–5 μm and 8–14 μm , respectively) it exhibited a designable narrowband absorption, and its peak wavelengths were simultaneously controlled by altering the width of the grating stripe. Shorter wavebands also exhibited certain higher order resonance modes that exhibited relative low absorption peaks. The absorption peaks of the designed microstructure merely included odd resonance modes under normal incidence, whereas the missing even modes were only observed under oblique incidence. We adopted different methods to fit the phase shifts, and subsequently calculated the resonance wavelengths by F–P and MIM theories. The results were well in agreement with the values obtained by the FDTD method, thereby verifying the validity of our simulations. This multilayer grating provides a new method for generating a Si-based device with multiple working bands in infrared.

Acknowledgments

This project was supported by the National Natural Science Foundation of China (Nos. U1435210, 61675199).

References

- [1] P.F. Li, B.A. Liu, Y.Z. Ni, K.K. Liew, J. Sze, S. Chen, S. Shen, Large-scale nanophotonic solar selective absorbers for high-efficiency solar thermal energy conversion, *Adv. Mater.* 27 (2015) 4585.
- [2] G. Ariyawansa, V. Apalkov, A.G.U. Perera, S.G. Matsik, G. Huang, P. Bhattacharya, Bias-selectable tricolor tunneling quantum dot infrared photodetector for atmospheric windows, *Appl. Phys. Lett.* 92 (2008) 111104.
- [3] A. Tittl, A.K.U. Michel, M. Schäferling, X.H. Yin, B. Gholipour, L. Cui, M. Wuttig, T. Taubner, F. Neubrech, H. Giessen, A switchable mid-infrared plasmonic perfect absorber with multispectral thermal imaging capability, *Adv. Mater.* 27 (2015) 4597.
- [4] B. Fazio, P. Artoni, M.A. Iati, C. D’Andrea, M.J.L. Faro, S.D. Sorbo, S. Pirotta, P.G. Gucciardi, P. Musumeci, C.S. Vasi, R. Saija, M. Galli, F. Priolo, A. Irrera, Strongly enhanced light trapping in a two-dimensional silicon nanowire random fractal array, *Light Sci. Appl.* 5 (2016) e16062.

- [5] P. Zhang, S.B. Li, C.H. Liu, X.B. Wei, Z.M. Wu, Y.D. Jiang, Z. Chen, Near-infrared optical absorption enhanced in black silicon via Ag nanoparticle-induced localized surface plasmon, *Nanoscale Res. Lett.* 9 (2014) 519.
- [6] Y. Wang, Y.P. Liu, H.L. Liang, Z.X. Mei, X.L. Du, Broadband antireflection on the silicon surface realized by Ag nanoparticle-patterned black silicon, *Phys. Chem. Chem. Phys.* 15 (2013) 2345.
- [7] J. Yang, F.F. Luo, T.S. Kao, X. Li, G.W. Ho, J.H. Teng, X.G. Luo, M.H. Hong, Design and fabrication of broadband ultralow reflectivity black Si surfaces by laser micro/nanoprocessing, *Light Sci. Appl.* 3 (2014) e185.
- [8] Z.H. Huang, J.E. Carey, M.G. Liu, X.Y. Guo, E. Mazura, J.C. Campbell, Micro-structured silicon photodetector, *Appl. Phys. Lett.* 89 (2006) 033506.
- [9] C.H. Crouch, J.E. Carey, M. Shen, E. Mazur, F.Y. Génin, Infrared absorption by sulfur-doped silicon formed by femtosecond laser irradiation, *Appl. Phys. A* 79 (2004) 1635.
- [10] Q. Sun, K. Ueno, H. Yu, A. Kubo, Y. Matsuo, H. Misawa, Direct imaging of the near field and dynamics of surface plasmon resonance on gold nanostructures using photoemission electron microscopy, *Light Sci. Appl.* 2 (2013) e118.
- [11] A. Sobhani, M.W. Knight, Y. Wang, B. Zheng, N.S. King, L.V. Brown, Z. Fang, P. Nordlander, N.J. Halas, Narrowband photodetection in the near-infrared with a plasmon-induced hot electron device, *Nature Commun.* 4 (2013) 1643.
- [12] M.W. Knight, Y.M. Wang, A.S. Urban, A. Sobhani, B.Y. Zheng, P. Nordlander, N.J. Halas, Embedding plasmonic nanostructure diodes enhances hot electron emission, *Nano Lett.* 13 (2013) 1687.
- [13] A.N. Mohammad, B.A. Fatih, B.T. Berk, K.O. Ali, Random sized plasmonic nanoantennas on silicon for low-cost broad-band nearinfrared photodetection, *Sci. Rep.* 4 (2014) 7103.
- [14] J.M. Hao, J. Wang, X.L. Liu, W.J. Padilla, L. Zhou, M. Qiu, High performance optical absorber based on a plasmonic metamaterial, *Appl. Phys. Lett.* 96 (2010) 251104.
- [15] Y.R. Qu, Q. Li, H.M. Gong, K.K. Du, S.A. Bai, D. Zhao, H. Ye, M. Qiu, Spatially and spectrally resolved narrowband optical absorber based on 2D grating nanostructures on metallic films, *Adv. Opt. Mater.* 4 (2016) 480.
- [16] X.C. Ma, Y. Dai, L. Yu, B.B. Huang, Energy transfer in plasmonic photocatalytic composites, *Light Sci. Appl.* 5 (2016) e16017.
- [17] M.W. Knight, H. Sobhani, P. Nordlander, N.J. Halas, Photodetection with active optical antennas, *Science* 332 (2011) 702.
- [18] W. Li, J. Valentine, Metamaterial perfect absorber based hot electron photodetection, *Nano Lett.* 14 (2014) 3510.
- [19] K.T. Lin, H.L. Chen, Y.S. Lai, C.C. Yu, Silicon-based broadband antenna for high responsivity and polarization-insensitive photodetection at telecommunication wavelengths, *Nature Commun.* 5 (2014) 3288.
- [20] Y.H. Su, Y.F. Ke, S.L. Cai, Q.Y. Yao, Surface plasmon resonance of layer-by-layer gold nanoparticles induced photoelectric current in environmentally-friendly plasmon-sensitized solar cell, *Light Sci. Appl.* 1 (2012) e14.
- [21] D.X. Ji, H.M. Song, X. Zeng, H.F. Hu, K. Liu, N. Zhang, Q.Q. Gan, Broadband absorption engineering of hyperbolic metafilm patterns, *Sci. Rep.* 4 (2014) 4498.
- [22] Y.X. Cui, S.L. He, Enhancing extraordinary transmission of light through a metallic nanoslit with a nanocavity antenna, *Opt. Lett.* 34 (2009) 16.
- [23] L.W. Fu, P. Schau, K. Frenner, W. Osten, Mode coupling and interaction in a plasmonic microcavity with resonant mirrors, *Phys. Rev. B* 84 (2011) 235402.
- [24] D. Zhao, L.J. Meng, H.M. Gong, X.X. Chen, Y.T. Chen, M. Yan, Q. Li, M. Qiu, Ultra-narrow-band light dissipation by a stack of lamellar silver and alumina, *Appl. Phys. Lett.* 104 (2014) 221107.
- [25] F. Hu, H. Yi, Z. Zhou, Band-pass plasmonic slot filter with band selection and spectrally splitting capabilities, *Opt. Express* 19 (2011) 4848.
- [26] M. Bora, E.M. Behymer, D.A. Dehlinger, J.A. Britten, C.C. Larson, A.S.P. Chang, K. Munechika, H.T. Nguyen, T.C. Bond, Plasmonic black metals in resonant nanocavities, *Appl. Phys. Lett.* 102 (2013) 251105.
- [27] J. Petschulat, C. Helgert, M. Steinert, N. Bergner, C. Rockstuhl, F. Lederer, T. Pertsch, A. Tünnermann, E.B. Kley, Plasmonic modes of extreme subwavelength nanocavities, *Opt. Lett.* 35 (2010) 2693.
- [28] X.Y. Liu, J.S. Gao, H.G. Yang, X.Y. Wang, Si-based near-infrared narrowband absorber based on square Au patches, *J. Opt. Soc. Amer. B* 33 (2016) 2149.